Petroleum Science 20 (2023) 2784–2795

Contents lists available at ScienceDirect

Petroleum Science

journal homepage: www.keaipublishing.com/en/journals/petroleum-science

Original Paper

Stable attenuation-compensated reverse time migration and its application to land seismic data

Xin-Ru Mu [a, b], Qiang Mao [a, b], Jian-Ping Huang [a, b, *]

[a] Geosciences Department, China University of Petroleum (East China), Qingdao, Shandong, 266580, China
[b] Pilot National Laboratory for Marine Science and Technology (Qingdao), Qingdao, Shandong, 266000, China

ARTICLE INFO

Article history:
Received 10 August 2022
Received in revised form
27 December 2022
Accepted 17 March 2023
Available online 21 March 2023

Edited by Jie Hao

Keywords:
Seismic attenuation
Reverse time migration
Stability strategy
Pseudospectral method

ABSTRACT

Intrinsic attenuation of the earth causes energy loss and phase distortion in seismic wave propagation. To obtain high-resolution imaging results, these negative effects must be considered during reverse time migration (RTM). We can easily implement attenuation-compensated RTM using the constant Q viscoacoustic wave equation with decoupled amplitude attenuation and phase dispersion terms. However, the nonphysical amplitude-compensation process will inevitably amplify the high-frequency noise in the wavefield in an exponential form, causing the numerical simulation to become unstable. This is due to the fact that the amplitude of the compensation grows exponentially with frequency. In order to achieve stable attenuation-compensated RTM, we modify the analytic expression of the attenuation compensation extrapolation operator and make it only compensate for amplitude loss within the effective frequency band. Based on this modified analytic formula, we then derive an explicit time-space domain attenuation compensation extrapolation operator. Finally, the implementation procedure of stable attenuation-compensated RTM is presented. In addition to being simple to implement, the newly proposed attenuation-compensated extrapolation operator is superior to the conventional low-pass filter in suppressing random noise, which will further improve the imaging resolution. We use two synthetic and one land seismic datasets to verify the stability and effectiveness of the proposed attenuation-compensated RTM in improving imaging resolution in viscous media.

1. Introduction

It has been observed that the intrinsic attenuation of the earth is widely distributed in the subsurface layers (Kjartansson, 1979; Aki and Richards, 1980; Carcione, 2007; Bai et al., 2013). For example, the seismic wave will exhibit significant attenuation characteristics as it travels through the gas chimneys or gas-saturated shale formations (Zhang et al., 2010; Zhu et al., 2014). If the amplitude attenuation and phase dispersion of seismic waves are not corrected during migration imaging, the imaging amplitude will be weaken and the imaging resolution will be reduced. Therefore, it is necessary to develop a corresponding prestack depth migration imaging method to correct these effects in viscoacoustic media and obtain more interpretable imaging results.

There are some mathematical and physical models to describe seismic attenuation, such as the constant Q attenuation model ((Kjartansson, 1979; Aki and Richards, 1980) and the superposition of standard linear solid (SLS) elements (Carcione et al., 1988; Zhu et al., 2013). In the initial application stage of correcting the effects of viscosity, geophysicists usually used the inverse Q filtering method to compensate for seismic attenuation (Wang, 2002, 2006). However, because it is based on a 1D model, this approach is incapable of dealing with complex subsurface structures. Therefore, the ray theory based (Traynin et al., 2008; Xie et al., 2009; Yue et al., 2021), one-way wave equation based (Zhang and Wapenaar, 2002; Shen et al., 2018; Mu et al., 2021), and two-way wave equation based migration imaging methods were proposed to correct attenuation effects over the past two decades. The two-way wave equation-based reverse time migration (RTM), which can handle complex models with steep dip layers, is regarded to be the most precise imaging technique among these (Deng and McMechan, 2007; Zhu et al., 2014; Yang and Zhu, 2018).

* Corresponding author. Geosciences Department, China University of Petroleum (East China), Qingdao, Shandong, 266580, China.
E-mail addresses: xinrumu@126.com (X.-R. Mu), jphuang@upc.edu.cn (J.-P. Huang).

https://doi.org/10.1016/j.petsci.2023.03.014

For implementing RTM applications with amplitude compensation and phase correction, many time- and frequency-domain viscoacoustic wave equations have been proposed to describe the effect of viscosity on seismic wave propagation (e.g., Emmerich and Korn, 1987; Liao and McMechan, 1996; Carcione et al., 1998; Operto et al., 2007; Zhu and Harris, 2014; Bai et al., 2014; Yang and Zhu, 2018). It is simple to simulate viscoacoustic wave propagation in the frequency domain by incorporating a frequency-dependent complex-valued velocity into the frequency-domain acoustic wave equation (Liao and McMechan, 1996; Operto et al., 2007; Sourbier et al., 2011). However, due to the high computational cost and complex numerical solutions, these frequency-domain viscoacoustic equations are rarely used in the petroleum industry for imaging and inversion. Because of its simple numerical solution and minimal calculation, the viscoacoustic wave equation in the time domain is more commonly used in practice. The viscoacoustic wave equation based on the SLS model is a common time-domain viscoacoustic wave equation that is frequently used as the forward and backward propagation operator in attenuation compensation RTM (Carcione et al., 1998; Zhu et al., 2013; Dutta and Schuster, 2014; Fathalian et al., 2020). This type of viscoacoustic wave equation can be solved using the high-efficiency finite difference (FD) method, but it contains coupled phase dispersion and amplitude loss terms, making attenuation-compensated RTM not straightforward to implement. Based on Kjartansson's constant Q (CQ) attenuation model, several time-domain viscoacoustic wave equations with fractional space derivative are proposed (Carcione, 2010; Zhu and Harris, 2014; Mu et al., 2021). The appearance of the viscoacoustic equation with decoupled amplitude attenuation and phase dispersion terms set off a hot wave of research on migration imaging and velocity inversion for viscous media in industrial applications. A great deal of research work has been done on the derivation of the high precision viscoacoustic wave equation based on the constant Q model (Mu et al., 2021), the numerical solution of the variable spatial fractional Laplace operators (Chen et al., 2016, 2019; Li et al., 2016; Zhang et al., 2020; Zhao et al., 2020; Mu et al., 2022a; Wang et al., 2022a), and the application of RTM and full waveform inversion (Sun et al., 2015; Sun and Zhu, 2018; Chen et al., 2021).

Given that high-frequency noise is exponentially amplified during the amplitude compensation process, the final imaging results will be unstable if we do not introduce some other stabilization strategies (Li et al., 2019; Liu et al., 2020; Mu et al., 2022b). Many stability strategies have been proposed and applied to imaging seismic data with good results. It is the easiest stabilization method to obtain stable imaging results by using a low-pass filter to suppress high-frequency noise in the wavefield (Zhu et al., 2014; Zhu and Harris, 2015; Sun et al., 2015). However, for complex models with sharp velocity contrast, the low-pass filter will damage some effective signals and reduce the image quality. Incorporating a regularization operator to stabilize seismic wave propagation is another typical stabilization technique (Tian et al., 2015; Qu et al., 2017; Zhao et al., 2018). This approach provides explicit expressions and is simple to numerically implement. By deriving the adjoint operator of the viscoacoustic wave equation and constructing a least-squares migration method, one can also obtain stable imaging results (Dutta and Schuster, 2014; Yang and Zhu, 2019). Nevertheless, this iterative method requires huge computation costs in practical applications. The stabilization factor method seems to be a better stability strategy, which can realize adaptive attenuation compensation in the time-space domain (Wang, 2006; Wang et al., 2018, 2022b; Chen et al., 2020). Mu et al. (2022) recently proposed a wave propagation stabilization method that uses a regulatory factor to limit the frequency range of attenuation compensation to the effective frequency band.

To obtain high-resolution imaging results in viscoaoustic media, it is of great significance to establish a stable and accurate attenuation-compensated RTM. Because the constant Q viscoacoustic wave equation comprises decoupled amplitude attenuation and phase dispersion terms, the attenuation-compensated extrapolation formula can be constructed by simply reversing the sign of the amplitude attenuation component while keeping the sign of the dispersion term unchanged. However, the amplitude compensation grows exponentially with frequency, causing severe oscillation in the high-frequency wavefields and ultimately the instability of the migration imaging result. On the basis of the stability method proposed by Mu et al. (2022), we evaluate a new stable attenuation compensation analytical expression, which can better protect the effective signal. Then a stable attenuation compensation simulation formula is developed by combining the relation between wavenumber and angular frequency derived by Mu et al. (2021) with the analytical expression of attenuation compensation. This proposed attenuation compensation simulation formula can efficiently suppress the high-frequency noises. Finally, we build an attenuation-compensated RTM in accordance with the source-normalized cross-correlation imaging condition. Synthetic and field data tests show that the proposed attenuation-compensated RTM method is stable and efficient in compensating amplitude loss and correcting phase dispersion.

This paper is organized as follows. First, we review the decoupled fractional-order viscoacoustic wave equation. Then, we derive a stable viscoacoustic attenuation-compensated propagation formula. After that, the numerical methods for solving the viscoacoustic wave equation and the attenuation-compensated propagation formula are illustrated. Finally, we show the robustness and adaptability of the newly developed attenuation-compensated RTM algorithm by using two synthetic and one field datasets.

2. Methodology

2.1. Framework of the attenuation-compensated RTM

Similar to acoustic RTM, viscoacoustic RTM also includes three procedures: forward propagation of the point sources; backward propagation of the received shot gathers; and applying imaging conditions. For the cross-correlation imaging condition, amplitude compensation is required in both forward and backward propagation processes, while for the source-normalized cross-correlation imaging condition, attenuation compensation is needed only in the wavefield backpropagation process. The source-normalized cross-correlation condition is better because the amplitude compensation simulation is invariably followed by the application of a stabilization operator, and any stabilization operator will alter the wavefield information (Zhu, 2016). Therefore, in this paper, we construct the attenuation-compensated RTM workflow based on the source-normalized cross-correlation condition.

In attenuating media, the energy attenuation during seismic wave propagation can be expressed by an exponential rate $e^{-\alpha L}$, where α is the attenuation factor and L denotes the propagation distance. As seen in Fig. 1a, seismic wave is excited by the source and travels downward. After hitting a reflection layer, this wave will return to the surface and be detected by a surface-deployed detector. In this process, the total energy attenuation is $e^{-\alpha L_{\text{down}}} e^{-\alpha L_{\text{up}}}$, where L_{down} and L_{up} are the propagation distances of the downgoing and upgoing waves, respectively. The received wavefield reflected from a certain subsurface point $\mathbf{x}$ can be expressed as $R^F(\mathbf{x}, t) = R(\mathbf{x}, t) e^{-\alpha L_{\text{down}}} e^{-\alpha L_{\text{up}}}$, where $R(\mathbf{x}, t)$ represents the received wavefield in non-attenuating media, t is the time variable of seismic wave propagation.

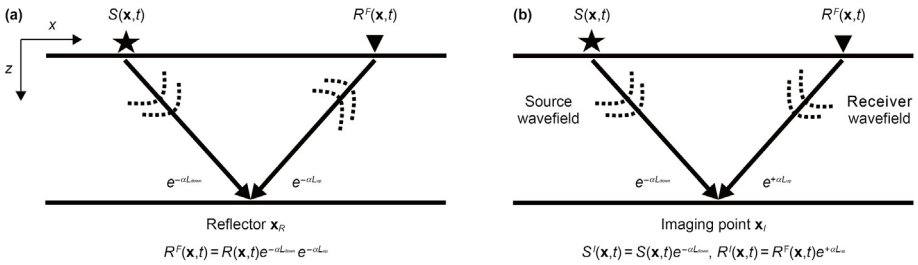

Fig. 1. Seismic wave propagation paths and mathematical representation for amplitude attenuation and compensation: Forward simulation (a) and RTM (b).

For attenuation-compensated RTM with source-normalized cross-correlation imaging condition, the source wavefield is attenuated and the receiver wavefield is compensated as shown in Fig. 1b (Zhu, 2016). Thus, the source wavefield at the imaging point $\mathbf{x}_I$ can be represented by $S^I(\mathbf{x},t) = S(\mathbf{x},t)e^{-\alpha L_{\text{down}}}$, where $S(\mathbf{x},t)$ denotes the source wavefield in non-attenuating media. The receiver wavefield at the imaging point $\mathbf{x}_I$ is defined by $R^I(\mathbf{x},t) = R^F(\mathbf{x},t)e^{+\alpha L_{\text{up}}}$. As a consequence, the source-normalized cross-correlation imaging condition in attenuating media is written as

$$I(\mathbf{x}) = \frac{\int_0^{T_{\max}} S^I(\mathbf{x},t)R^I(\mathbf{x},t)\mathrm{d}t}{\int_0^{T_{\max}} S^I(\mathbf{x},t)S^I(\mathbf{x},t)\mathrm{d}t} = \frac{\int_0^{T_{\max}} S(\mathbf{x},t)R(\mathbf{x},t)\mathrm{d}t}{\int_0^{T_{\max}} S(\mathbf{x},t)S(\mathbf{x},t)\mathrm{d}t}, \tag{1}$$

where $T_{\max}$ is the total recording time of the shot gather. Theoretically, we can use Eq. (1) to provide imaging results in attenuating media that are identical in amplitude and phase to those produced in non-attenuating media.

2.2. Review of the viscoacoustic wave equation

In this section, we will briefly introduce the derivation of the viscoacoustic wave equation. In exploration geophysics, attenuation is considered to be nearly linear with frequency, and many mathematical and physical models have been proposed to describe the CQ attenuation (McDonal et al., 1958; Kjartansson, 1979; Aki and Richards, 1980). Based on Kjartansson's CQ model, the complex phase velocity of viscoacoustic media in the frequency domain can be expressed as (Carcione et al., 2002)

$$v = \sqrt{\frac{M}{\rho}}, \tag{2}$$

where ρ is the density, the complex function $M(\omega) = M_0(i\omega/\omega_0)^{2\gamma}$ and $M_0 = \rho v_0^2 \cos^2(\pi\gamma/2)$, ω denotes angular frequency and ω_0 represents reference angular frequency, v_0 is the phase velocity defined at ω_0, $\gamma = \arctan(1/Q)/\pi$, the value of γ is (0, 0.5) for any positive quality factor Q.

By replacing the velocity variable in the frequency-wavenumber domain acoustic wave equation with Eq. (2), we can easily obtain the CQ viscoacoustic wave equation (Aki and Richards, 1980; Liao and McMechan, 1996; Yang and Zhu, 2018)

$$\omega^2 = v_0^2 \cos^2(\pi\gamma/2)\left(\frac{i\omega}{\omega_0}\right)^{2\gamma}\mathbf{k}^2, \tag{3}$$

where $\mathbf{k}$ denotes the complex-valued wavenumber.

After making some derivations for Eq. (3), Mu et al. (2021) constructed a time domain CQ viscoacoustic wave equation that includes decoupled terms in describing amplitude attenuation and phase dispersion. It can be expressed as

$$\frac{\omega^2}{v_1^2} = \eta\mathbf{k}^{2\gamma+2} + \tau(i\omega)\mathbf{k}^{\gamma+1}, \tag{4}$$

where $v_1 = v_0\cos(\pi\gamma/2)$, $\eta = v_0^{2\gamma}\cos(\pi\gamma)\omega_0^{-2\gamma}\cos^{2\gamma}(\frac{\pi\gamma}{2})$ and $\tau = v_0^{\gamma-1}\sin(\pi\gamma)\omega_0^{-\gamma}\cos^{\gamma-1}(\frac{\pi\gamma}{2})$. Note that this equation has higher accuracy in describing CQ attenuation than the one derived by Zhu and Harris (2014).

By transforming Eq. (4) into the time-space domain, it can be written as

$$\frac{1}{v_1^2}\frac{\partial^2 p}{\partial t^2} = -\eta\left(-\nabla^2\right)^{\gamma+1}p - \frac{\partial}{\partial t}\tau\left(-\nabla^2\right)^{\gamma/2+1/2}p + f_s, \tag{5}$$

where f_s denotes source time function, p represents pressure wavefield in the time-space domain.

To illustrate the amplitude attenuation and phase dispersion effects clearly, we further reformulate Eq. (5) as

$$\frac{1}{v_1^2}\frac{\partial^2 p}{\partial t^2} = \nabla^2 p + \beta_1\left\{-\eta\left(-\nabla^2\right)^{\gamma+1} - \nabla^2\right\}p - \beta_2\frac{\partial}{\partial t}\tau\left(-\nabla^2\right)^{\gamma/2+1/2}p + f_s. \tag{6}$$

Equation (6) becomes an acoustic wave equation if β_1 and β_2 are both 0. If we only simulate the amplitude attenuation characteristics, then we can assume $\beta_1 = 0$ and $\beta_2 = 1$. Conversely, if $\beta_1 = 1$ and $\beta_2 = 0$, only the phase dispersion feature is simulated. When $\beta_1 = 1$ and $\beta_2 = 1$, Eq. (6) simulates both amplitude attenuation and phase dispersion effects.

2.3. Derivation of the stable attenuation-compensated extrapolation formula

By reversing the sign of the amplitude attenuation term while keeping the phase dispersion term unchanged (i.e., $\beta_1 = 1$ and $\beta_2 = -1$), the attenuation-compensated wave equation can be written as (Zhu et al., 2014)

$$\frac{1}{v_1^2}\frac{\partial^2 p}{\partial t^2} = \nabla^2 p + \left\{-\eta\left(-\nabla^2\right)^{\gamma+1} - \nabla^2\right\}p + \frac{\partial}{\partial t}\tau\left(-\nabla^2\right)^{\gamma/2+1/2}p + f_r, \tag{7}$$

where f_r denotes the received seismic data. The high-frequency noise in the wavefield will increase exponentially if we employ Eq. (7) directly for attenuation compensation simulation, leading to numerical instability of the imaging results.

According to seismic wave propagation theory, the energy of a seismic wave propagating in a viscous medium decays exponentially with propagation distance. This relationship can be described mathematically and physically as (Wang, 2002, 2006)

$$p(x+\Delta x,\omega)=p(x,\omega)\exp[-ik_c(\omega)\Delta x], \tag{8}$$

where Δx denotes the propagation distance, $k_c(\omega)$ denotes the complex-valued dispersion relation of the frequency-independent attenuation model (Kjartansson, 1979) and can be represented by

$$k_c(\omega)=\frac{\omega_0^{\gamma}\omega^{1-\gamma}e^{-i\pi\gamma/2}}{v_0\cos(\pi\gamma/2)}, \tag{9}$$

where the real term is used to simulate phase dispersion, while the imaginary part describes amplitude decay. Therefore, the corresponding analytical solution of seismic wave propagation with amplitude compensation and phase dispersion is described as (Mu et al., 2022b)

$$p(x+\Delta x,\omega)=p(x,\omega)\exp\left[-i\left(k_c^{r}(\omega)-ik_c^{i}(\omega)\right)\Delta x\right], \tag{10}$$

where k_c^{r} and k_c^{i} represent the real and imaginary components of k_c, respectively. By substituting Eq. (9) into Eq. (10) and using a relationship $\Delta t=\Delta x/v_0$, we can obtain

$$p(t+\Delta t,\omega)=p(t,\omega)\exp\left[\Delta t\omega_0^{\gamma}\omega^{1-\gamma}\tan(\pi\gamma/2)\right]\cdot\exp\left[-i\Delta t\omega_0^{\gamma}\omega^{1-\gamma}\right]. \tag{11}$$

In Eq. (11), the exponential term with an imaginary part describes the phase dispersion, and the exponential term with a real part represents the amplitude compensation. In addition, Eq. (11) shows that the amplitude amplification process is a frequency-dependent exponential growth function. To avoid amplifying high-frequency noise, we consider modifying Eq. (11) so that the attenuation compensation process can only be performed in the effective frequency band range. We add a stabilization term $2(1-\sigma\omega)$ to Eq. (11), and the attenuation compensation formula can be written as (Mu et al., 2022b)

$$p(t+\Delta t,\omega)=p(t,\omega)\exp\left[2\Delta t\omega_0^{\gamma}\omega^{1-\gamma}(1-\sigma\omega)\tan(\pi\gamma/2)\right], \tag{12}$$

where σ denotes the stabilization factor. The exponential term in Eq. (12) is approximately a quadratic function of ω and we can regulate the amplitude compensation frequency range by altering the stabilization factor σ. The symmetry axis of this approximated amplitude compensation function (i.e., exponential term of Eq. (12)) is

$$\omega_\sigma=\frac{1}{2\sigma},\ \left(\text{i.e.,}\ \sigma=\frac{1}{2\omega_\sigma}\right). \tag{13}$$

By altering the stabilization factor σ, the high-frequency components can be suppressed, as shown by the variations of attenuation compensation with frequency in Fig. 2. In Fig. 2, the solid lines are calculated by the exponential term of Eq. (12), and the solid red line indicates attenuation compensation without the stabilization scheme. The quality factor, Δt, and the reference frequency are 60, 1 ms and 30 Hz, respectively. From Fig. 2, we can observe that the wavefield components with an angular frequency less than $2\omega_\sigma$ are compensated, while those with an angular frequency greater than $2\omega_\sigma$ are suppressed. In other words, the wavefields within the effective frequency band are compensated, while those outside the effective frequency band are suppressed.

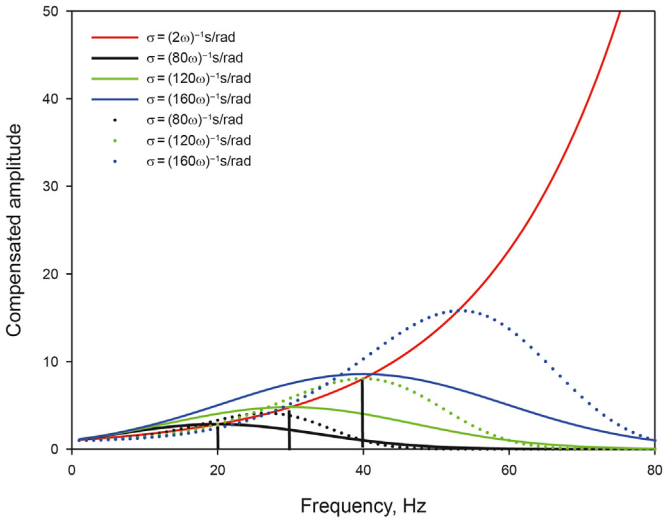

Fig. 2. Attenuation compensation varies with frequency for different stabilization factors. The solid lines are calculated by the exponential term of Eq. (12), whereas the dashed lines are calculated by the exponential term of Eq. (14). Note that the solid red line indicates attenuation compensation without the stabilization scheme.

As shown in Fig. 2, there are errors between the amplitude compensation simulation formula described by Eq. (12) and the exact amplitude compensation simulation formula. To obtain more accurate attenuation compensation wavefields, we modify Eq. (12) as

$$p(t+\Delta t,\omega)=p(t,\omega)\exp\left[\Re\Delta t\omega_0^{\gamma}\omega^{1-\gamma}(1-\sigma\omega)\omega\tan(\pi\gamma/2)\right], \tag{14}$$

where $\Re$ is a σ-dependent constant value, which can be determined by the relation that

$$\exp\left[\Re\Delta t\omega_0^{\gamma}\omega^{1-\gamma}(1-\sigma\omega)\omega\tan(\pi\gamma/2)\right]|_{\omega=\omega_{\max}} \equiv\exp\left[\Delta t\omega_0^{\gamma}\omega^{1-\gamma}\tan(\pi\gamma/2)\right]|_{\omega=\omega_{\max}}, \tag{15}$$

when $\omega=\omega_{\max}$, the left term of Eq. (15) reaches its maximum value and $\Re=1/((1-\sigma\omega_{\max})\omega_{\max})$.

Similarly, we use the exponential term from Eq. (14) to plot the characteristics of amplitude compensation, which are shown as dashed lines in Fig. 2. The improved formula (Eq. (14)) describes amplitude compensation more precisely than Eq. (12), as seen in Fig. 2. Based on Eq. (14), we obtain the analytical equation with stable attenuation compensation and phase correction effects as

$$p(t+\Delta t,\omega)=p(t,\omega)\exp\left[\Re\Delta t\omega_0^{\gamma}\omega^{1-\gamma}(1-\sigma\omega)\omega\tan(\pi\gamma/2)\right]\cdot\exp\left[-i\Delta t\omega_0^{\gamma}\omega^{1-\gamma}\right]. \tag{16}$$

The dispersion relation associated with Eq. (16) can be written as

$$k_c(\omega)=v_0^{-1}\omega_0^{\gamma}\omega^{1-\gamma}\left(i\Re\omega\tan(\pi\gamma/2)-i\sigma\Re\omega^2\tan(\pi\gamma/2)+1\right). \tag{17}$$

After some mathematical derivations, we obtain the

corresponding approximate complex velocity of Eq. (17) as

$$v_p(\omega) = v_0\omega_0^{-\gamma}\omega^{\gamma}\Big(-i\Big(\Re\omega\tan(\pi\gamma/2) - \sigma\Re\omega^2\tan(\pi\gamma/2)\Big) + 1\Big). \tag{18}$$

Similarly, by replacing the velocity of the frequency-wavenumber domain acoustic equation with Eq. (18), we can derive a stable attenuation-compensated extrapolation formula

$$\omega^2 P = v_0^2\omega_0^{-2\gamma}\omega^{2\gamma}\begin{pmatrix} -\Re^2\omega^2\tan^2(\pi\gamma/2) - \sigma^2\Re^2\omega^4\tan^2(\pi\gamma/2) \\ +2\Re^2\omega^3\sigma\tan^2(\pi\gamma/2) + 1 \\ -2i\Re\omega\tan(\pi\gamma/2) + 2i\sigma\Re\omega^2\tan(\pi\gamma/2) \end{pmatrix}\mathbf{k}^2 P, \tag{19}$$

where P denotes the frequency-wavenumber wavefield. Note that the value of $\Re$ is only related to the choice of the stability factor σ and decreases as σ decreases. When σ equals $(80\pi)^{-1}$s/rad, we can use Eq. (15) to calculate $\Re$ and it equals 0.0181. Since the value of $\Re$ is very small, the terms related to the second power of $\Re$ can be ignored in Eq. (19) to reduce the computational burden. As a result, we ignore the second-order term associated with $\Re$ in the following derivations.

In the literature of Zhu and Harris (2014) and Mu et al. (2021), there are three approximate formulas that can be written as

$$\omega \approx v_0 k,\ \omega^{2\gamma} \approx v_0^{2\gamma}\cos^{2\gamma}(\pi\gamma/2)k^{2\gamma},\ i\omega^{2\gamma} \approx i\omega v_0^{\gamma-1}\cos^{\gamma-1}(\pi\gamma/2)\omega_0^{\gamma}k^{\gamma-1}. \tag{20}$$

Substituting Eq. (20) into Eq. (19) yields

$$\omega^2 P = \Big(\xi_1 k^{2\gamma+2} + \xi_2(i\omega)k^{2\gamma+2} + \xi_3(i\omega)k^{\gamma+3}\Big)P, \tag{21}$$

where $\xi_1 = v_0^{2\gamma+2}\omega_0^{-2\gamma}\cos^{2\gamma}(\pi\gamma/2)$, $\xi_2 = -2\Re\tan(\pi\gamma/2)v_0^{2\gamma+2}\omega_0^{-2\gamma}\cos^{2\gamma}(\pi\gamma/2)$, and $\xi_3 = 2\sigma\Re\tan(\pi\gamma/2)v_0^{\gamma+3}\omega_0^{-\gamma}\cos^{\gamma-1}(\pi\gamma/2)$.

By transforming Eq. (21) from the frequency-wavenumber domain into the time-space domain, we obtain

$$\frac{\partial^2 p}{\partial t^2} = -\Big(\xi_1\big(-\nabla^2\big)^{\gamma+1} + \xi_2\frac{\partial}{\partial t}\big(-\nabla^2\big)^{\gamma+1} + \xi_3\frac{\partial}{\partial t}\big(-\nabla^2\big)^{\gamma/2+1.5}\Big)p + f_r. \tag{22}$$

It should be noted that the stable attenuation compensation modeling equation proposed in this paper has an explicit expression (Eq. (22)) and will not significantly increase the computational cost over the amplitude attenuation simulation formula (Eq. (5)).

2.4. Method for determining ω_σ

The choice of cutoff angular frequency ω_σ is determined by the model's complexity and the frequency band range of seismic data. A low value of ω_σ will result in undercompensation. A high value of ω_σ will result in overcompensation. Synthetic tests show that cutoff angular frequency ω_σ should be larger than the dominant angular frequency of the wavelet in order to obtain accurate attenuation compensation imaging results. It can be calculated using an expression $\omega_\sigma = 2\pi(f_m + f_a)$, where f_m represents the main frequency of the source time function and f_a denotes the frequency increment (usually $5 < f_a < 20$). An accurate ω_σ can be determined by the following two steps. First, we simulate the wavefield propagation using a stable attenuation compensation extrapolation operator based on a low-pass filter (Zhu, 2016) and use the simulated wavefield as a reference. We then use Eq. (22) to simulate the amplitude compensated wavefield. The value of ω_σ is adjusted until the simulated wavefield is the most similar to the reference wavefield possible. In this case, the value of ω_σ is the final optimal value. After determining ω_σ, σ can be computed by Eq. (13).

3. Numerical implement

Some methods have been proposed for solving the spatial variable fractional Laplacian operators in Eqs. (5) and (22). For example, the average Q strategy (Zhu and Harris, 2014), low-rank approximation method (Sun et al., 2015), Hermite distributed approximation method (Yao et al., 2017), and fractional-order operator approximation scheme (Li et al., 2016; Chen et al., 2016; Zhang et al., 2020). Here, we decouple the wavenumber and fractional-order by using the second-order Taylor series expansion (TSE) to represent the variable fractional Laplacians (Zhang et al., 2020). The approximation of the mixed-domain operators $k^{2\gamma}$ and k^{γ} can be described as

$$\begin{aligned} k^{2\gamma} &\approx 1 + 2\ln(k)\gamma + 2\ln(k)^2\gamma^2\ (k>0), \\ k^{\gamma} &\approx 1 + \ln(k)\gamma + 0.5\ln(k)^2\gamma^2\ (k>0), \end{aligned} \tag{23}$$

By inserting Eq. (23) into Eq. (5) and transforming it from the wavenumber domain to the time domain, we can obtain the approximate time-wavenumber domain viscoacoustic wave equation as

$$\frac{\partial^2 p}{\partial t^2} = -v_1^2\Big(\eta\Big(1 + 2\ln(k)\gamma + 2\ln(k)^2\gamma^2\Big)k^2 + \tau(i\omega)\Big(k + \gamma\ln(k)k + \gamma^2\ln(k)^2 k/2\Big)\Big)P^w + f_s, \tag{24}$$

where P^w denoted the time-wavenumber domain expression of p. By means of the pseudospectrum method (PSM), Eq. (24) can be reformulated as

$$\frac{\partial^2 p}{\partial t^2} = -v_1^2\begin{pmatrix} \eta\Big(F^{-1}\Big[k^2F(p)\Big] + 2\gamma F^{-1}\Big[k^2\ln(k)F(p)\Big] + 2\gamma^2F^{-1}\Big[k^2\ln(k)^2F(p)\Big]\Big) \\ +\tau\left(F^{-1}\left[kF\left(\frac{\partial p}{\partial t}\right)\right] + \gamma F^{-1}\left[k\ln(k)F\left(\frac{\partial p}{\partial t}\right)\right] + \gamma^2F^{-1}\left[k\frac{\ln(k)^2}{2}F\left(\frac{\partial p}{\partial t}\right)\right]\right) \end{pmatrix} + f_s. \tag{25}$$

Similar to Eq. (5), the attenuation-compensated extrapolation formula (Eq. (22)) can be solved by PSM as

$$\frac{\partial^2 p}{\partial t^2} = -\begin{pmatrix} \xi_1\left(F^{-1}\left[k^2F(p)\right] + 2\gamma F^{-1}\left[k^2\ln(k)F(p)\right] + 2\gamma^2F^{-1}\left[k^2\ln(k)^2F(p)\right]\right) \\ +\xi_2\left(F^{-1}\left[k^2F\left(\frac{\partial p}{\partial t}\right)\right] + 2\gamma F^{-1}\left[k^2\ln(k)F\left(\frac{\partial p}{\partial t}\right)\right] + 2\gamma^2F^{-1}\left[k^2\ln(k)^2F\left(\frac{\partial p}{\partial t}\right)\right]\right) \\ +\xi_3\left(F^{-1}\left[k^3F\left(\frac{\partial p}{\partial t}\right)\right] + \gamma F^{-1}\left[k^3\ln(k)F\left(\frac{\partial p}{\partial t}\right)\right] + 0.5\gamma^2F^{-1}\left[k^3\ln(k)^2F\left(\frac{\partial p}{\partial t}\right)\right]\right) \end{pmatrix} + f_r. \tag{26}$$

4. Synthetic tests and field data application

In this section, two synthetic and one land seismic dataset tests are used to demonstrate the effectiveness of the proposed attenuation-compensated RTM. Before running RTM, we smooth the true models and use them as the migration models. For numerical simulation, the 500 m wide sponge absorbing boundary is used to attenuate boundary reflections on four boundaries (Cerjan et al., 1985). We also mute the direct waves to obtain clean imaging results.

4.1. Layered attenuation model

We first use a simple layered velocity model to demonstrate the effectiveness of our method in compensating amplitude attenuation and correcting phase dispersion. The layered attenuation model is shown in Fig. 3, which contains a low-Q anomaly in the middle of the model. There will be strong attenuation of seismic waves that propagate through the low-Q anomaly. The model has 401 × 201 grid points. The grid spacing is 10 m in the x- and z-directions. To generate synthetic data, Eq. (5) is used and 81 shots are evenly spaced at a depth of 10 m. In addition, a total of 401 receivers are evenly distributed on both sides of the source to receive the reflections. The receivers are also located below the surface at a depth of 10 m. A Ricker wavelet with a dominant frequency of 25 Hz is used as the source time function. The reference frequency in this example is 500 Hz. The records last 2 s and the time interval is 0.001 s. For the simulation of the common shot gathers without attenuation, we also use Eq. (5) by assuming $Q \rightarrow \infty$.

Fig. 4a–c displays the acoustic RTM image obtained by using acoustic data (reference imaging result), the acoustic RTM image obtained by using viscoacoustic data, and the proposed attenuation-compensated RTM image obtained by using viscoacoustic data, respectively. The ω_σ is 70π rad/s in this test. In Fig. 4b, the deeper layers below the anomaly exhibit weaker amplitudes compared with Fig. 4a. After attenuation compensation correction, the weak amplitudes are recovered as shown in Fig. 4c. A more intuitive comparison (Fig. 5) is made by extracting single traces from Fig. 4. The black dashed line in Fig. 5 has a lower amplitude and a phase shift when compared to the blue solid line. In contrast, there is good agreement in both amplitude and phase between the blue solid line and the red dashed line. These findings show that our proposed attenuation-compensated RTM can effectively correct the influence of viscosity and produce accurate imaging results.

4.2. Marmousi model

To further verify the reliability and stability of the proposed attenuation-compensated RTM, we test the attenuation-compensated RTM on a more complex Marmousi model. The real velocity and Q models are depicted in Fig. 6a and b, respectively. In the shallow region of the model, there are three anomalies with extremely high attenuation, which are typically brought on by gas accumulation. The grid size of this model is 396 × 201, with grid intervals of 10 m in both the horizontal and vertical directions. The reference frequency is set to 25 Hz here. We use Fig. 6 to simulate synthetic common shot gathers. The total recording time is 2.0 s with a time sampling interval of 0.8 ms. A 25 Hz Ricker wavelet is used as the source time function. The fixed spread geometry contains 46 sources that are evenly distributed with a shot spacing size of 80 m and a shot depth of 10 m. For each shot, 369 surface-deployed receivers with a receiver interval of 10 m are used to record the reflections. The viscoacoustic shot gathers are calculated by Eq. (5). Accordingly, we can obtain the acoustic data by assuming that Q is infinite.

As shown in Fig. 7a, we perform acoustic RTM on the simulated acoustic data to obtain a reference imaging profile. Fig. 7b and c shows the imaging results of acoustic RTM and the proposed attenuation-compensated RTM with viscoacoustic data, respectively. For this example, the stabilization factor ω_σ is 65π rad/s. As shown in Fig. 7b, the imaging results of acoustic RTM have dimmed amplitudes and blurred structures due to the lack of attenuation compensation correction. In contrast, the attenuation-

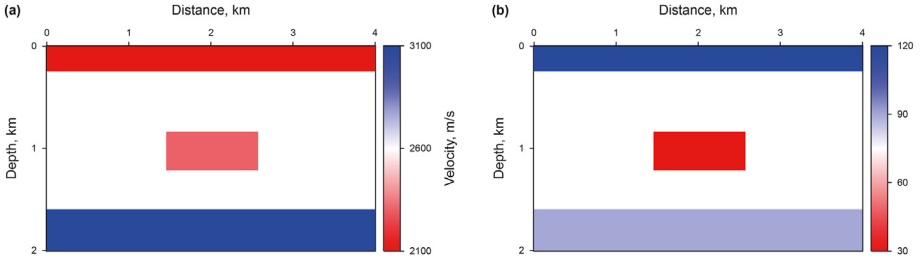

Fig. 3. A simple layer model. (a) velocity and (b) Q models.

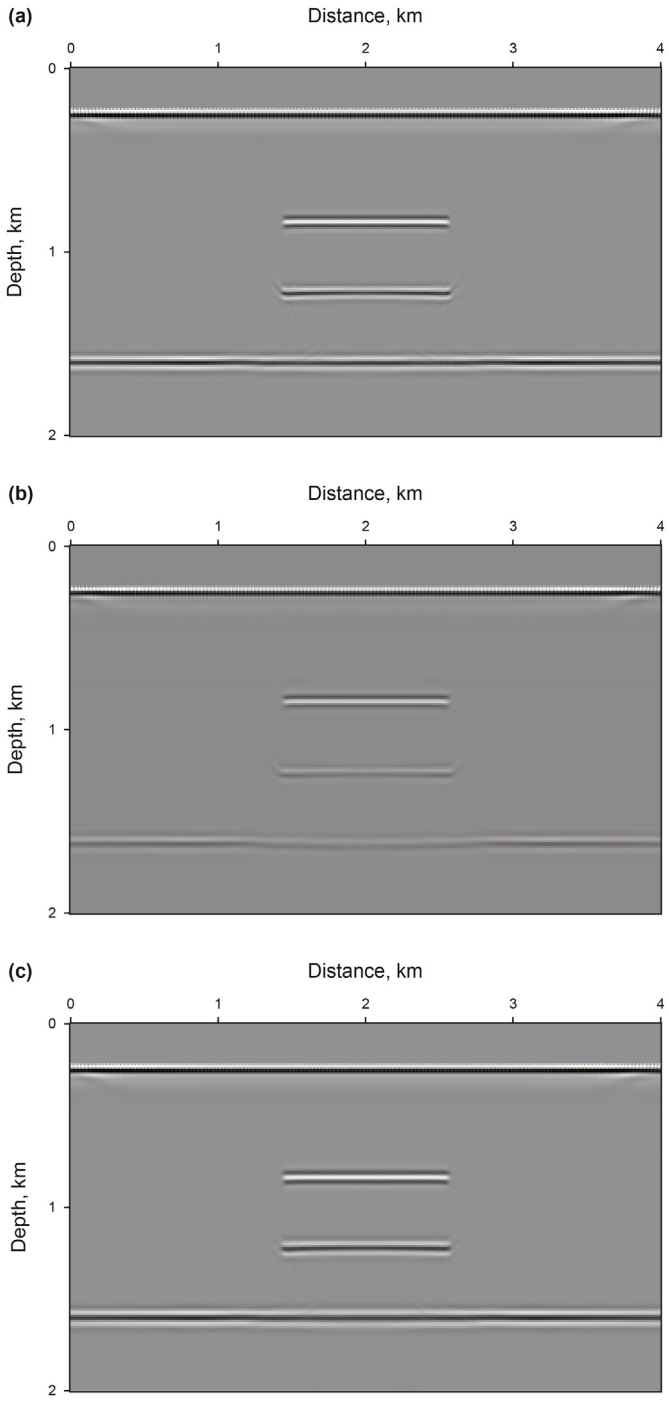

Fig. 4. (a) is obtained by using acoustic RTM on the simulated acoustic data (reference imaging result), (b) is obtained by using acoustic RTM on the simulated viscoacoustic data, and (c) is obtained by using the proposed attenuation-compensated RTM on the simulated viscoacoustic data.

compensated RTM imaging results (Fig. 7c) have mostly recovered the amplitude of the anticline structures. In order to demonstrate the advantages of the attenuation-compensated RTM in compensating amplitude attenuation and correcting phase dispersion in detail, as shown by Fig. 8, we compare the waveforms of single traces extracted from Fig. 7. In Fig. 8, we can clearly see that the red dashed line agrees well with the blue solid line (reference imaging result), while the black dashed line exhibits significantly lower amplitude and phase distortion compared with the reference trace. According to the comparison results, we can conclude that the proposed attenuation-compensated RTM can produce accurate imaging results in the complex attenuating media.

Fig. 7d shows the conventional attenuation-compensated RTM with a low-pass filter. The cutoff frequency for the low-pass filter is 120 Hz. Comparing Fig. 7c and d, we can observe that when there is no noise in the shot record, our attenuation-compensated RTM and the conventional attenuation-compensated RTM with a low-pass filter yield equivalent imaging results.

4.3. Land seismic data example

In this example, a real land seismic dataset is used to illustrate the effectiveness of our proposed attenuation-compensated RTM in improving imaging resolution and fidelity. The migration velocity and Q models are displayed in Fig. 9. The empirical formula $Q = 3.56v_0^{2.3}$ yields the Q model, with km/s serving as the unit of v_0. This model contains 2943 $\times$ 601 grid nodes with a grid spacing of 10 m in both the horizontal and vertical directions. The field data includes 63 shots with an equivalent shot spacing of 350 m. Each shot is recorded with 140 receivers, and the receiver interval is 50 m. The recording time is 3.6 s, and the time sampling interval is 0.6 ms. The excitation source is a Ricker wavelet with a peak frequency of 35 Hz. The reference frequency is 35 Hz. To stabilize wavefield propagation, the ω_σ is set to 72π rad/s in this test. Fig. 10 shows the imaging results obtained by using acoustic RTM and the proposed attenuation-compensated RTM, respectively. In comparison to Fig. 10a, the amplitude of Fig. 10b is more balanced in the middle and deep regions. Furthermore, the attenuation-compensated imaging results show better seismic event continuity than the acoustic RTM imaging results (indicated by the black dashed boxes and black arrows). According to the mean wavenumber spectra (Fig. 11) of the migration images shown in the dashed boxes in Fig. 10a and b, we can see that the frequency band has been widened after attenuation compensation. This demonstrates that RTM with attenuation compensation can improve imaging resolution when there is viscosity in the acquired seismic data.

5. Discussion

In this example, we want to evaluate the applicability of the new method to image noisy data. Here, we use the Marmousi model (Fig. 6) and the same synthetic data as those used in Fig. 7. In addition, Gaussian random noise is added to the synthetic common

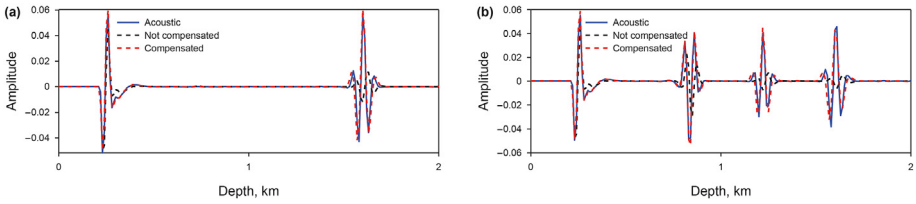

Fig. 5. Extracted vertical traces from Fig. 4 at a horizontal distance of 1.0 km (a) and 2 km (b), respectively. The blue, red, and black lines are extracted from Fig. 4a, b, and 4c, respectively.

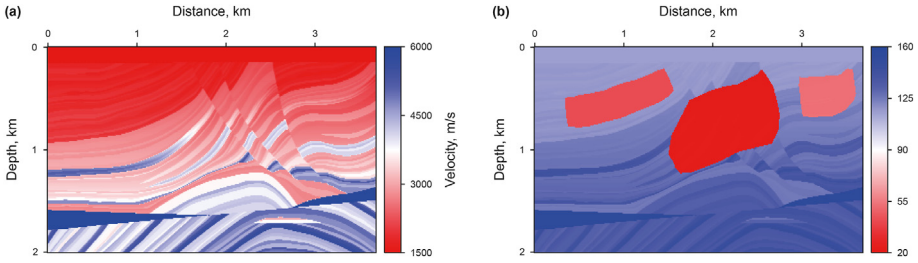

Fig. 6. The true Marmousi model includes (a) velocity and (b) *Q*.

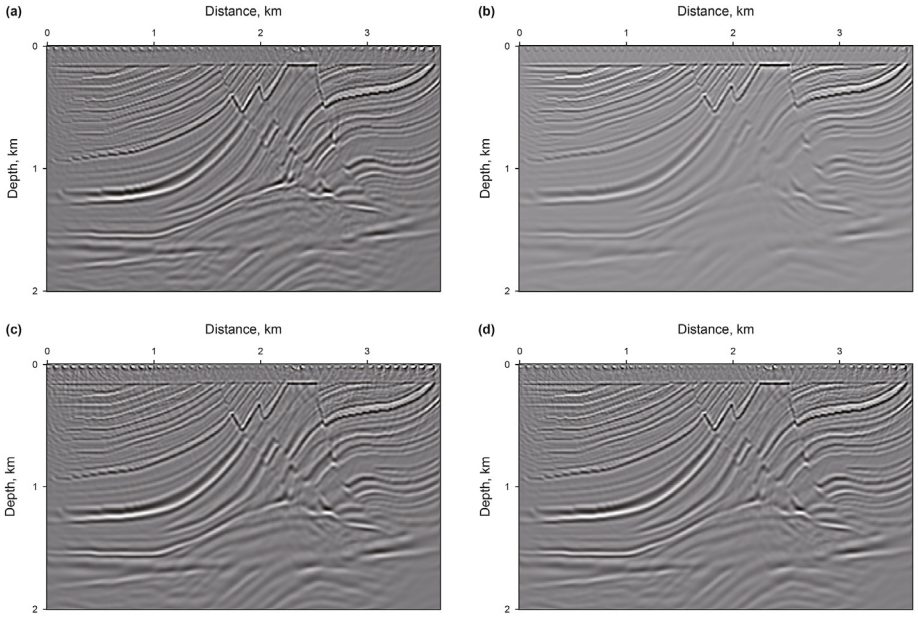

Fig. 7. (a) is the result of using acoustic RTM on simulated acoustic data (reference imaging result), (b) is the result of using acoustic RTM on simulated viscoacoustic data, (c) is the result of using the proposed attenuation-compensated RTM on simulated viscoacoustic data, and (d) is the result of using conventional attenuation-compensated RTM with a low-pass filter on simulated viscoacoustic data.

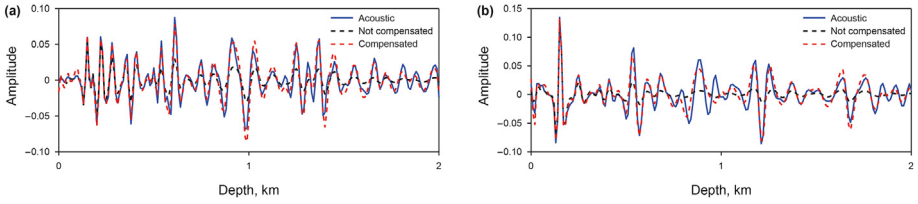

Fig. 8. Extracted vertical slices from Fig. 7 at a distance of 1.5 km (a) and 2.5 km (b), respectively. Vertical traces extracted from Fig. 7a, b, and 7c are represented by blue solid, red dashed, and black dashed lines, respectively.

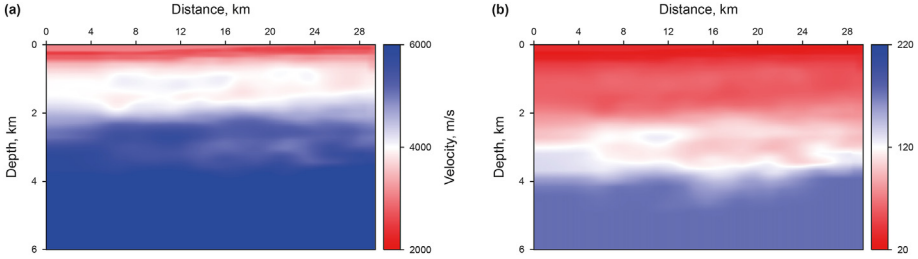

Fig. 9. Migration velocity (a) and (b) *Q* models for land seismic data.

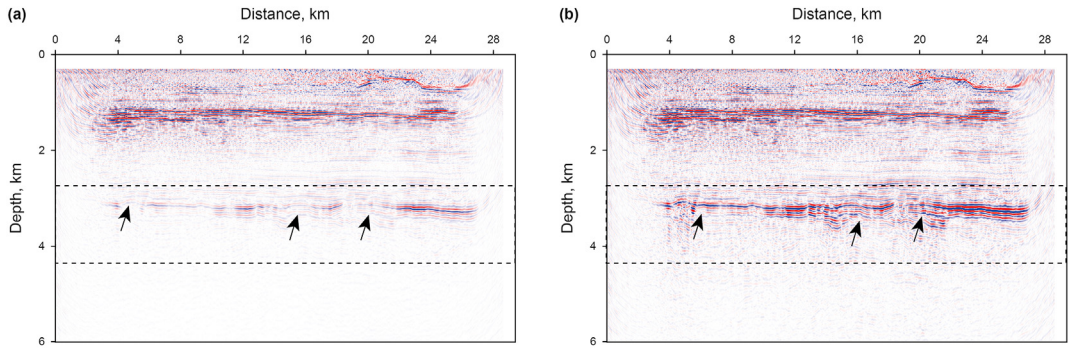

Fig. 10. Migration imaging results for the land seismic data obtained by using the (a) acoustic RTM and the (b) proposed attenuation-compensated RTM.

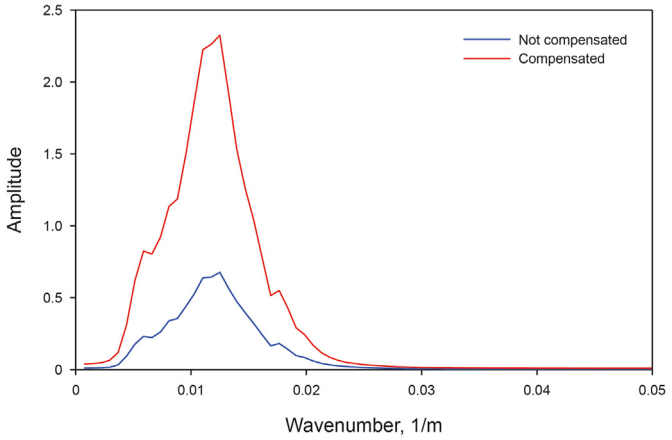

Fig. 11. The average wavenumber spectrum of the images shown in the dashed boxes in Fig. 10a and b. The migration images with and without compensation are represented by the red and blue lines, respectively.

shot gathers. The results obtained by the proposed attenuation-compensated RTM (PAC-RTM) are compared with those obtained by the conventional attenuation-compensated RTM (CAC-RTM) with a low-pass filter. It should be noted that the parameters used by the two migration imaging methods here are identical to those shown in Fig. 7.

Firstly, we add different amounts of high-frequency random noise to the noise-free shot gathers, and the signal to noise ratio (SNR) of the shot gathers after adding noise is 5 dB and 10 dB, respectively. It should be noted that the high-frequency noise spans 60–500Hz. Fig. 12 shows two noise-contaminated shot gathers with the same source but different SNRs, and the source is located at a distance of $x = 1.9$ km. According to Fig. 12, the effective signal energy increases as the SNR increases. We use these two built seismic datasets to perform attenuation-compensated RTM and the imaging results are shown in Fig. 13. Both conventional and newly proposed attenuation-compensated migration imaging methods can produce stable imaging results. The noise in imaging results gradually increases as SNR decreases. When compared to CAC-RTM imaging results (Fig. 13c and d), PAC-RTM imaging results (Fig. 13a

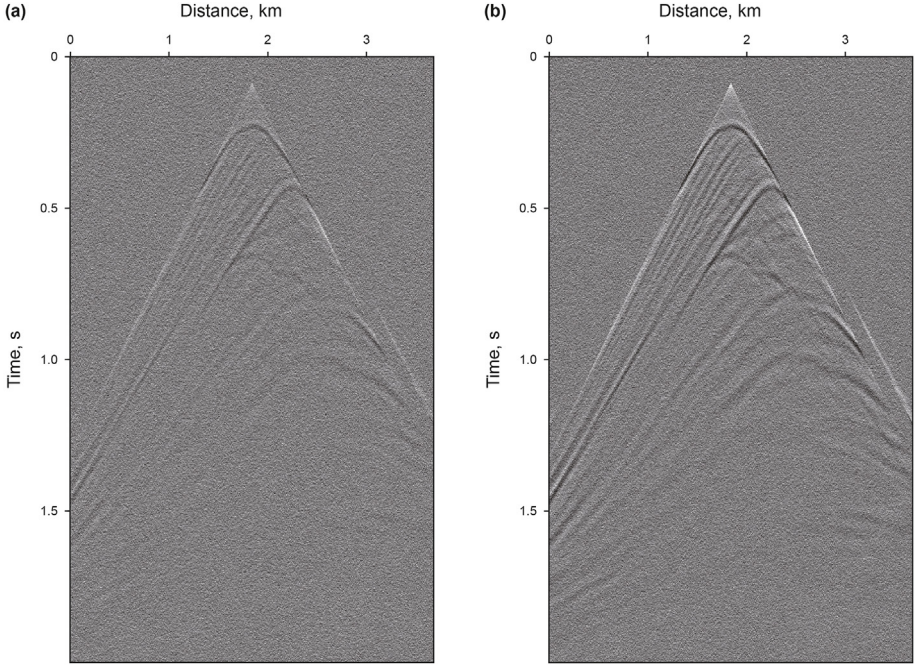

Fig. 12. Noise-contaminated shot gatherings and the SNR are (a) 5 dB and (b) 10 dB, respectively. Note that the direct waves of the shot gathers are muted and the frequency of random noise is greater than 60 Hz.

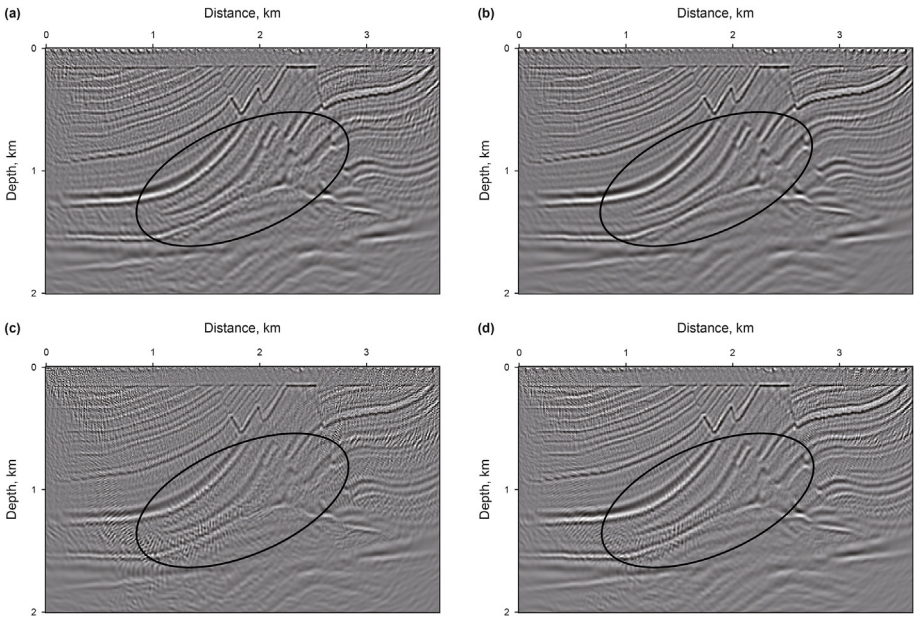

Fig. 13. Migration imaging results are obtained by (a and b) PAC-RTM and (c, d) CAC-RTM. The SNRs of the used seismic data are (a and c) 5 dB and (b and d) 10 dB, respectively.

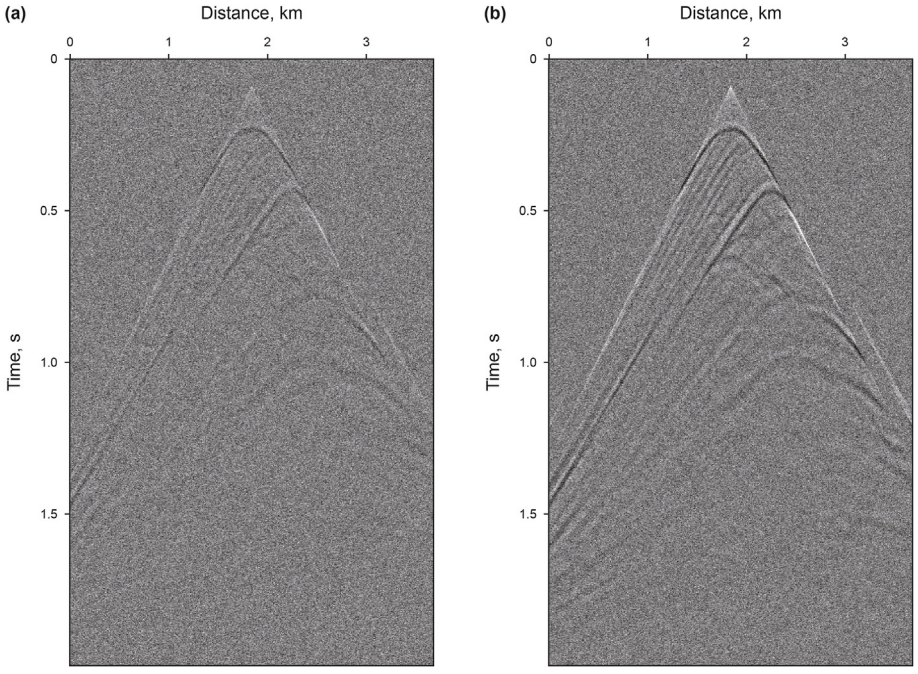

Fig. 14. Noise-contaminated shot gathers and the SNR are (a) 5 dB and (b) 10 dB, respectively. Note that the direct waves of the shot gathers are muted and the frequency of random noise is distributed within 0–500 Hz.

and b) have significantly less noise and higher resolution, particularly for anticline structures (indicated by the dashed elliptical box). This indicates, in suppressing high-frequency noise, the proposed attenuation-compensated RTM outperforms the conventional low-pass filter-based attenuation-compensated RTM.

To demonstrate the imaging quality of the new method when there are some random noises in the effective frequency band, random noise with a frequency band of 0–500 Hz is added to the noise-free shot gathers. Fig. 14 shows two noise-contaminated shot gathers with the same source location as those in Fig. 12 but different SNRs. The energy of the effective signal in Fig. 14 is weaker than that in Fig. 12 at the same SNR. Then we use CAC-RTM and PAC-RTM to image the seismic data with different SNR, and the imaging results are shown in Fig. 15. Compared with Fig. 13, it can be seen in Fig. 15 that the quality of imaging results deteriorates when the noise frequency distribution range widens. The imaging results in Fig. 15 show that the new method can successfully recover complex underground structures even when the data SNR is as low as 5. The CAC-RTM provides noisier imaging results than the PAC-RTM and performs poorly when imaging anticline structures. This demonstrates that, when compared to a low-pass filter, our stability strategy suppresses random noise better and produces more accurate imaging results.

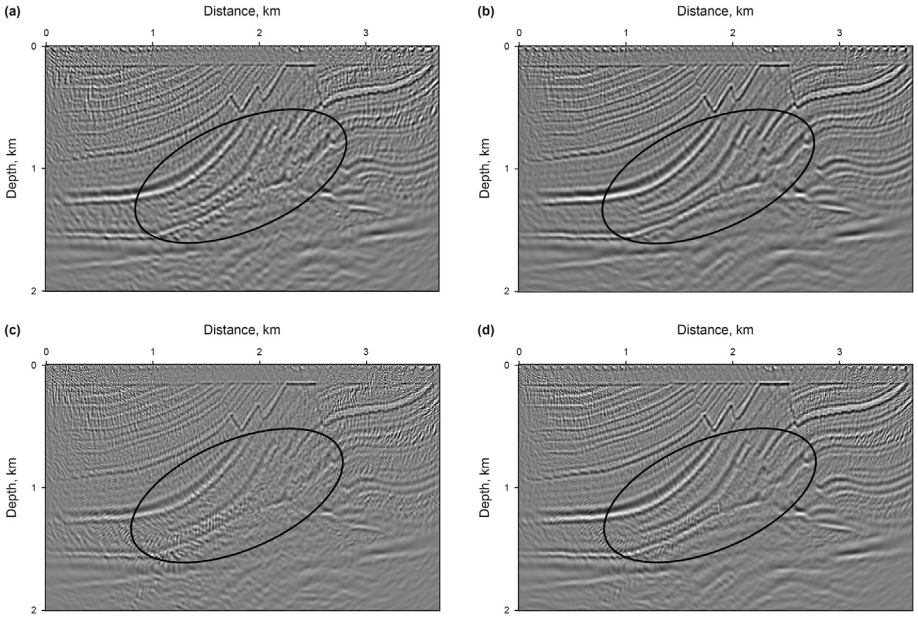

Fig. 15. Migration imaging results are obtained by (a and b) PAC-RTM and (c, d) CAC-RTM. The SNR of the used seismic data is (a and c) 5 dB and (b and d) 10 dB, respectively.

6. Conclusion

Compensating for anelastic effects during RTM is an attractive task for improving imaging resolution and balancing imaging amplitude. However, backward propagation of the viscoacoustic wavefield may lead to numerical instability due to tremendously increased high-frequency noise. Given that numerical instability is caused by overcompensation of the wavefield's high-frequency components, we first develop a stable attenuation compensation analytical expression that can suppress high-frequency noise while adequately protecting the effective signal. Then a stable attenuation compensation extrapolation operator is developed. The amplitude attenuation and the derived amplitude compensation simulation operators can be solved using the PSM. We then establish an attenuation-compensated RTM algorithm based on the source normalized cross-correlation imaging condition. Two synthetic and one land seismic dataset tests show that attenuation-compensated RTM can produce more balanced amplitude and higher resolution imaging results than non-compensated RTM.

Declaration of competing interest

The authors declare that they have no known competing financial interests, academic competition, intellectual passion, or personal relationships that could have appeared to influence the work reported in this paper.

Acknowledgements

We thank the editor and two anonymous reviewers for their insightful comments that significantly improved the quality of this paper. This study is supported by the Marine S&T Fund of Shandong Province for Pilot National Laboratory for Marine Science and Technology (Qingdao) (No. 2021QNLM020001), the Major Scientific and Technological Projects of Shandong Energy Group (No. SNKJ2022A06-R23), the Major Scientific and Technological Projects of CNPC (No. ZD2019-183-003).

References

Aki, K., Richards, P., 1980. Quantitative seismology: theory and methods. Freeman, San Francisco, CA. https://doi.org/10.1121/1.385057.
Bai, J., Chen, G., Yingst, D., et al., 2013. Attenuation compensation in viscoacoustic reverse-time migration. In: 83rd Annual International Meeting, SEG, Expanded Abstracts, pp. 3825–3830. https://doi.org/10.1190/segam2013-1252.1.
Bai, J., D Yingst, D., Bloor, R., et al., 2014. Viscoacoustic waveform inversion of velocity structures in the time domain. Geophysics 79 (3), R103–R119. https://doi.org/10.1190/geo2013-0030.1.
Carcione, J.M., 2007. Wave Fields in Real Media: Theory and Numerical Simulation of Wave Propagation in Anisotropic, Anelastic, Porous and Electromagnetic Media, second ed. Elsevier.
Carcione, J.M., 2010. A generalization of the Fourier pseudo-spectral method. Geophysics 75 (6), A53–A56. https://doi.org/10.1190/1.3509472.
Carcione, J.M., Kosloff, D., Kosloff, R., 1988. Wave propagation simulation in a linear viscoacoustic medium. Geophys. J. Int. 93 (2), 393–401. https://doi.org/10.1111/j.1365-246X.1988.tb02010.x.
Carcione, J.M., Helle, H.B., Tong, Z., 1998. Effects of attenuation and anisotropy on reflection amplitude versus offset. Geophysics 63 (5), 1652–1658. https://doi.org/10.1190/1.1444461.
Carcione, J.M., Cavallini, F., Mainardi, F., et al., 2002. Time domain seismic modeling of constant-Q wave propagation using fractional derivatives. Pure Appl. Geophys. 159 (7), 1719–1736. https://doi.org/10.1007/s00024-002-8705-z.
Cerjan, C., Kosloff, D., Kosloff, R., et al., 1985. A nonreflecting boundary condition for discrete acoustic and elastic wave equations. Geophysics 50 (4), 705–708. https://doi.org/10.1190/1.1441945.
Chen, H., Zhou, H., Li, Q., et al., 2016. Two efficient modeling schemes for fractional Laplacian viscoacoustic wave equation. Geophysics 81 (5), T233–T249. https://doi.org/10.1190/geo2015-0660.1.
Chen, H., Zhou, H., Rao, Y., et al., 2019. A matrix-transform numerical solver for fractional Laplacian viscoacoustic wave equation. Geophysics 84 (4), T283–T297. https://doi.org/10.1190/geo2018-0271.1.
Chen, H., Zhou, H., Rao, Y., 2020. An implicit stabilization strategy for Q-compensated reverse time migration. Geophysics 76 (5), WB97–WB107. https://doi.org/10.1190/geo2019-0235.1.
Chen, H., Zhou, H., Rao, Y., 2021. Source wavefield reconstruction in fractional Laplacian viscoacoustic wave equation-based full waveform inversion. IEEE Trans. Geosci. Rem. Sens. 59 (8), 6496–6509. https://doi.org/10.1109/TGRS.2020.3029630.
Deng, F., McMechan, G.A., 2007. True-amplitude prestack depth migration. Geophysics 72 (3), S155–S166. https://doi.org/10.1190/1.2714334.
Dutta, G., Schuster, G.T., 2014. Attenuation compensation for least squares reverse time migration using the viscoacoustic-wave equation. Geophysics 79 (6), S251–S262. https://doi.org/10.1190/geo2013-0414.1.
Emmerich, H., Korn, M., 1987. Incorporation of attenuation into time domain computations of seismic wave fields. Geophysics 52 (9), 1252–1264. https://doi.org/10.1190/1.1442386.
Fathalian, A., Trad, D., Innanen, K.A., 2020. An approach for attenuation-compensating multidimensional constant-Q viscoacoustic reverse time migration. Geophysics 85 (1), S33–S46. https://doi.org/10.1190/geo2019-0107.1.

Kjartansson, E., 1979. Constant-Q wave propagation and attenuation. J. Geophys. Res. 84 (B9), 4737–4748. https://doi.org/10.1029/JB084iB09p04737.
Li, Q., Zhou, H., Zhang, Q., et al., 2016. Efficient reverse time migration based on fractional Laplacian viscoacoustic wave equation. Geophys. J. Int. 204 (1), 488–504. https://doi.org/10.1093/gji/ggv456.
Li, Q., Fu, L., Zhou, H., et al., 2019. Effective Q-compensated reverse time migration using new decoupled fractional Laplacian viscoacoustic wave equation. Geophysics 84 (2), S57–S69. https://doi.org/10.1190/geo2017-0748.1.
Liao, Q., McMechan, G.A., 1996. Multifrequency viscoacoustic modeling and inversion. Geophysics 61 (5), 1371–1378. https://doi.org/10.1190/1.1444060.
Liu, Y.L., Li, Z.C., Wang, J., et al., 2020. Stable viscoacoustic reverse time migration in frequency domain for undulated shallow surface (in Chinese). Oil Geophys. Prospect. 55 (6), 1312–1320. https://doi.org/10.13810/j.cnki.issn.1000-7210.2020.06.017.
McDonal, F.J., Angona, F.A., Mills, R.L., et al., 1958. Attenuation of shear and compressional waves in Pierre shale. Geophysics 23 (3), 421–439. https://doi.org/10.1190/1.1438489.
Mu, X., Huang, J., Wen, L., et al., 2021. Modeling viscoacoustic wave propagation using a new spatial variable-order fractional Laplacian wave equation. Geophysics 86 (6), T487–T507. https://doi.org/10.1190/geo2020-0610.1.
Mu, X., Huang, J., Yang, J., et al., 2022a. Modeling of Pure visco-qP-wave propagation in attenuating tilted transversely isotropic (TTI) media based on decoupled fractional Laplacians. Geophysics 87 (4), A49–V277. https://doi.org/10.1190/geo2021-0440.1.
Mu, X., Huang, J., Li, Z., et al., 2022b. Attenuation compensation and anisotropy correction in reverse time migration for attenuating tilted transversely isotropic media. Surv. Geophys. 43 (3), 737–773. https://doi.org/10.1007/s10712-022-09707-2.
Operto, S., Virieux, J., Amestoy, P., et al., 2007. 3D finite-difference frequency-domain modeling of visco-acoustic wave propagation using a massively parallel direct solver: a feasibility study. Geophysics 72 (5), SM195–SM211. https://doi.org/10.1190/1.2759835.
Qu, Y., Huang, J., Li, Z., et al., 2017. Attenuation compensation in anisotropic least-squares reverse time migration. Geophysics 82 (6), S411–S423. https://doi.org/10.1190/geo2016-0677.1.
Shen, Y., Biondi, B., Clapp, R., 2018. Q-model building using one-way wave-equation migration Q analysis — Part 1: theory and synthetic test. Geophysics 83 (2), S93–S109. https://doi.org/10.1190/geo2016-0658.1.
Sourbier, F., Haidar, A., Giraud, L., et al., 2011. Three-dimensional parallel frequency-domain visco-acoustic wave modelling based on a hybrid direct/iterative solver. Geophys. Prospect. 59 (5), 834–856. https://doi.org/10.1111/j.1365-2478.2011.00966.x.
Sun, J., Zhu, T., 2018. Strategies for stable attenuation compensation in reverse-time migration. Geophys. Prospect. 66 (3), 498–511. https://doi.org/10.1111/1365-2478.12579.
Sun, J., Zhu, T., Fomel, S., 2015. Viscoacoustic modeling and imaging using low-rank approximation. Geophysics 80 (5), A103–A108. https://doi.org/10.1190/geo2015-0083.1.
Tian, K., Huang, J., Bu, C., et al., 2015. Viscoacoustic reverse time migration by adding a regularization term. In: 85th Annual International Meeting, SEG, Expanded Abstracts, pp. 4127–4131. https://doi.org/10.1190/segam2015-5932246.1.
Traynin, P., Liu, J., Reilly, J.M., 2008. Amplitude and bandwidth recovery beneath gas zones using Kirchhoff prestack depth Q-migration. In: 78th Annual International Meeting, SEG, Expanded Abstracts, pp. 2412–2416. https://doi.org/10.1190/1.3059363.
Wang, Y., 2002. A stable and efficient approach of inverse Q filtering. Geophysics 67 (2), 657–663. https://doi.org/10.1190/1.1468627.
Wang, Y., 2006. Inverse Q-filter for seismic resolution enhancement. Geophysics 71 (3), V51–V60. https://doi.org/10.1190/1.2192912.
Wang, Y., Zhou, H., Chen, H., et al., 2018. Adaptive stabilization for Q-compensated reverse time migration. Geophysics 83 (1), S15–S32. https://doi.org/10.1190/geo2017-0244.1.
Wang, N., Xing, G., Zhu, T., et al., 2022a. Propagating seismic waves in VTI attenuating media using fractional viscoelastic wave equation. J. Geophys. Res. Solid Earth 127 (4), e2021JB023280. https://doi.org/10.1029/2021JB023280.
Wang, N., Shi, Y., Zhou, H., 2022b. Accurately stable Q-compensated reverse-time migration scheme for heterogeneous viscoelastic media. Rem. Sens. 14 (19), 4782. https://doi.org/10.3390/rs14194782.
Xie, Y., Xin, K., Sun, J., et al., 2009. 3D prestack depth migration with compensation for frequency dependent absorption and dispersion. In: 79th Annual International Meeting, SEG, Expanded Abstracts, pp. 2919–2922. https://doi.org/10.1190/1.3255457.
Yang, J., Zhu, H., 2018. Viscoacoustic reverse time migration using a time-domain complex-valued wave equation. Geophysics 83 (6), S505–S519. https://doi.org/10.1190/geo2018-0050.1.
Yang, J., Zhu, H., 2019. Viscoacoustic least-squares reverse time migration using a time-domain complex-valued wave equation. Geophysics 84 (5), S479–S499. https://doi.org/10.1190/geo2018-0804.1.
Yao, J., Zhu, T., Hussain, F., et al., 2017. Locally solving fractional Laplacian viscoacoustic wave equation using Hermite distributed approximating functional method. Geophysics 82 (2), T59–T67. https://doi.org/10.1190/geo2016-0269.1.
Yue, Y., Liu, Y., Li, Y., et al., 2021. Least-squares Gaussian beam migration in viscoacoustic media. Geophysics 86 (1), S17–S28. https://doi.org/10.1190/geo2020-0129.1.
Zhang, J., Wapenaar, K., 2002. Wavefield extrapolation and prestack depth migration in anelastic inhomogeneous media. Geophys. Prospect. 50 (6), 629–643. https://doi.org/10.1046/j.1365-2478.2002.00342.x.
Zhang, Y., Zhang, P., Zhang, H., 2010. Compensating for visco-acoustic effects in reverse-time migration. In: 80th Annual International Meeting, SEG, Expanded Abstracts, pp. 3160–3164. https://doi.org/10.1190/1.3513503.
Zhang, Y., Liu, Y., Xu, S., 2020. Arbitrary-order Taylor series expansion-based viscoacoustic wavefield simulation in 3D vertical transversely isotropic media. Geophys. Prospect. 68 (8), 2379–2399. https://doi.org/10.1111/1365-2478.12999.
Zhao, Y., Mao, N., Ren, Z., 2018. A stable and efficient approach of Q reverse time migration. Geophysics 83 (6), S557–S567. https://doi.org/10.1190/geo2018-0022.1.
Zhao, X., Zhou, H., Chen, H., et al., 2020. Domain decomposition for large-scale viscoacoustic wave simulation using localized pseudo-spectral method. IEEE Trans. Geosci. Rem. Sens. 59 (3), 2666–2679. https://doi.org/10.1109/TGRS.2020.3006614.
Zhu, T., 2016. Implementation aspects of attenuation compensation in reverse-time migration. Geophys. Prospect. 64 (3), 657–670. https://doi.org/10.1111/1365-2478.12301.
Zhu, T., Harris, J.M., 2014. Modeling acoustic wave propagation in heterogeneous attenuating media using decoupled fractional Laplacians. Geophysics 79 (3), T105–T116. https://doi.org/10.1190/geo2013-0245.1.
Zhu, T., Harris, J.M., 2015. Improved seismic image by Q-compensated reverse time migration: application to crosswell field data, west Texas. Geophysics 80 (2), B61–B67. https://doi.org/10.1190/geo2014-0463.1.
Zhu, T., Carcione, J.M., Harris, J.M., 2013. Approximating constant-Q seismic propagation in the time domain. Geophys. Prospect. 61 (5), 931–940. https://doi.org/10.1111/1365-2478.12044.
Zhu, T., Harris, J.M., Biondi, B., 2014. Q-compensated reverse-time migration. Geophysics 79 (3), S77–S87. https://doi.org/10.1190/geo2013-0344.1.